Full-Field Brillouin Microscopy with a Scanning Fabry-Perot Interferometer

- Supplementary materials -

- 1. Principles of Brillouin light scattering (BLS)
- 2. Optical setup for Full-Field Brillouin Microscopy
- 3. Data processing and precision estimation
- 4. Consequences of Suboptimal FPI Design and Rationalization of Spectral Measurement Outcomes
- 5. Estimating Spatial Resolution
- 6. Performance comparison of selected Brillouin imaging systems

1. Principles of Brillouin Light Scattering

Brillouin light scattering (BLS) is an inelastic light-scattering process that probes thermally induced acoustic waves—phonons—within a material [1–3]. These pressure waves travel at speeds determined by the mechanical properties of the medium. As light interacts with these propagating fluctuations, it is scattered with a frequency shift—known as the Brillouin shift—that encodes information about the viscoelastic response of the sample. A typical experimental configuration is illustrated in **Fig. S1a**, where the laser beam is focused into the sample, and scattered light is collected at a specific angle θ .

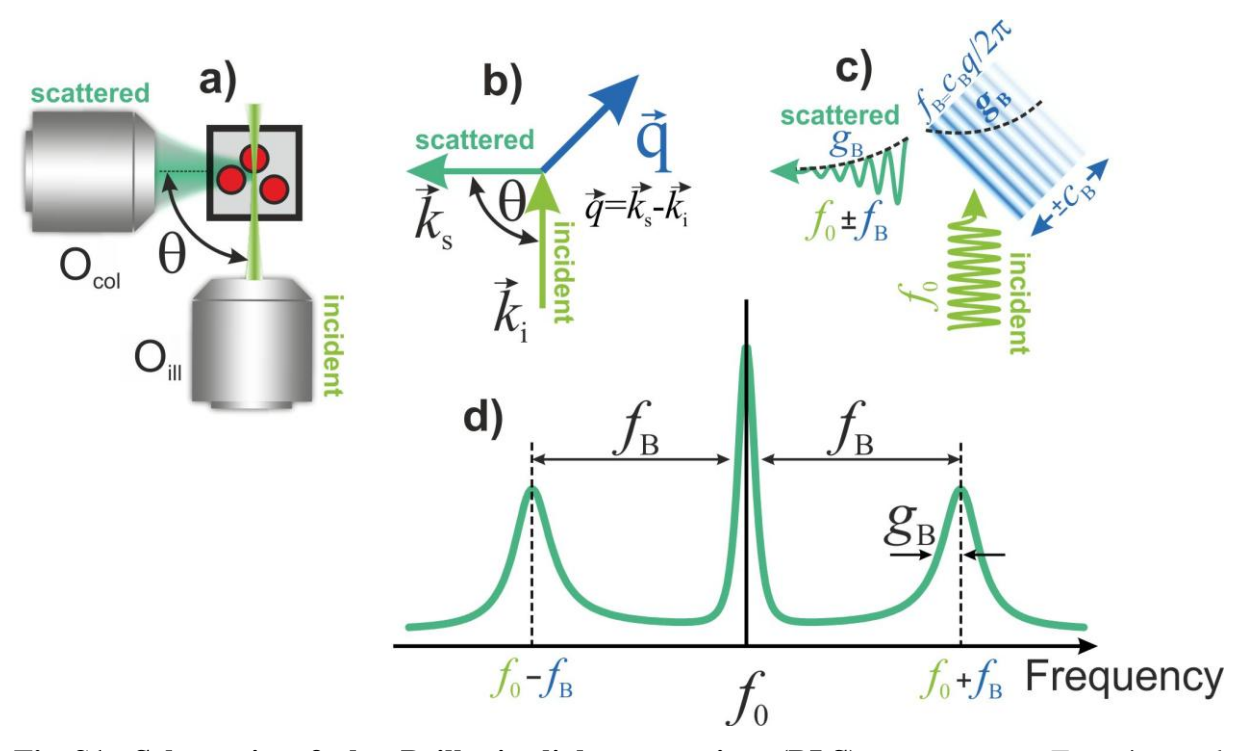


Fig. S1. Schematic of the Brillouin light scattering (BLS) process. a, Experimental configuration: A monochromatic laser beam (frequency f_0) is focused into the sample by the illumination objective (O_{ill}). Scattered light is collected by the detection objective (O_{col}),

forming a typical Brillouin scattering geometry. **b**, Definition of wavevectors: k_i and k_s are the wave-vectors of the incident and scattered light, respectively. The scattering wave-vector q is defined as the difference $q = k_s - k_i$ and represents the wave-vector of the acoustic phonon involved in the scattering process. The magnitude of q depends on the scattering angle θ , defined as the angle between k_i and k_s . **c**, Inelastic scattering mechanism: The incident light of frequency f_0 interacts with a thermally excited acoustic phonon of frequency f_B , propagating at velocity c_B in the direction given by q. The phonon has a finite lifetime, τ , characterized by its decay rate $g_B \approx 1/\tau$, due to viscous losses in the medium. The scattered light carries this information: its frequency is shifted by f_B (Doppler shift), and its spectral width reflects the decay rate g_B . **d**, Schematic Brillouin spectrum: The scattered light spectrum exhibits two symmetric peaks—the Stokes and anti-Stokes lines—shifted from the laser frequency f_0 by $\pm f_B$. The Brillouin shift f_B is directly related to the acoustic velocity c_B , while the linewidth g_B provides a measure of acoustic attenuation and is used to estimate the longitudinal viscosity η_B .

Mechanical Properties from BLS

The speed of these thermally excited sound waves, denoted c_B , depends on the medium's compressibility β (or its longitudinal elastic modulus M') and its mass density ρ :

$$c_B^2 = 1/\beta \rho = M'/\rho \tag{S1}$$

Rather than measuring c_B directly, Brillouin spectroscopy determines it from the Brillouin frequency shift f_B , which arises due to the Doppler effect as light scatters off moving acoustic waves. This scattering process and its wave-vector geometry are shown in **Fig. S1b**. The incident and scattered light define a scattering wave-vector \mathbf{q} , which sets the acoustic wavelength Λ that is probed. The frequency shift is related to the sound wave speed through:

$$c_B = f_B \Lambda \tag{S2}$$

The scattering wave-vector \mathbf{q} is defined by the wavelength of light, λ , the scattering angle θ , and the refractive index n:

$$q = 2\pi / \Lambda = \frac{4\pi n}{\lambda} \sin(\theta / 2)$$
 (S3)

Combining (S2) and (S3), the speed of sound is calculated as:

$$c_B = \frac{2\pi f_B}{q} \tag{S4}$$

This speed can be used to estimate the sample's compressibility or longitudinal modulus (Eq. S1). The physical mechanism behind the Brillouin frequency shift is depicted in **Fig. S1c**, where incident light interacts with a propagating sound wave, leading to frequency-shifted scattered light. In addition to stiffness, the sample's viscosity contributes to the acoustic wave behavior. Viscous damping causes the phonon to decay in time, resulting in a broadened Brillouin peak. The linewidth g_B (half width at half maximum) is directly related to the longitudinal kinematic viscosity η_B :

$$\eta_B = \frac{4\pi g_B}{q^2} \tag{S5}$$

These spectral features are observed experimentally as shown in **Fig. S1d**, which illustrates a typical Brillouin spectrum with two symmetric peaks (Stokes and anti-Stokes) flanking the laser frequency. The peak positions reflect the sound speed, and their width is proportional to the viscosity.

Reduced Quantities

Accurate estimation of mechanical properties requires knowledge of the refractive index n, which may be unknown and spatially varying in biological samples. To address this, we define reduced quantities that bypass this dependency. The reduced wave-vector q_n omits the refractive index:

$$q_n = \frac{4\pi}{\lambda} \sin(\theta/2) \tag{S6}$$

This leads to definitions of reduced mechanical parameters: reduced speed of sound, nc_B , (the produce between refractive index and speed of sound) as well as reduced longitudinal viscosity, $n^2\eta_B$, (the product of the square of refractive index and longitudinal viscosity) respectively as:

$$nc_B = \frac{2\pi f_B}{q_n} \tag{S7}$$

$$n^2 \eta_B = \frac{4\pi g_B}{q_n^2} \tag{S8}$$

These parameters are directly retrieved from measured spectral data and allow meaningful mechanical mapping without requiring independent refractive index measurements.

2. Optical Setup for Full-Field Brillouin Imaging

To implement Full-Field Brillouin Imaging (FFBI), we adapted a commercial multi-pass Tandem Fabry–Perot Interferometer [4] (TFPI-2, Sandercock-type), originally designed for single-point spectroscopy, into a two-dimensional spectral imaging platform. The system relies on light-sheet illumination, orthogonal collection, and tunable frequency filtering using the TFPI. A schematic of the optical setup is shown in **Fig. S2**.

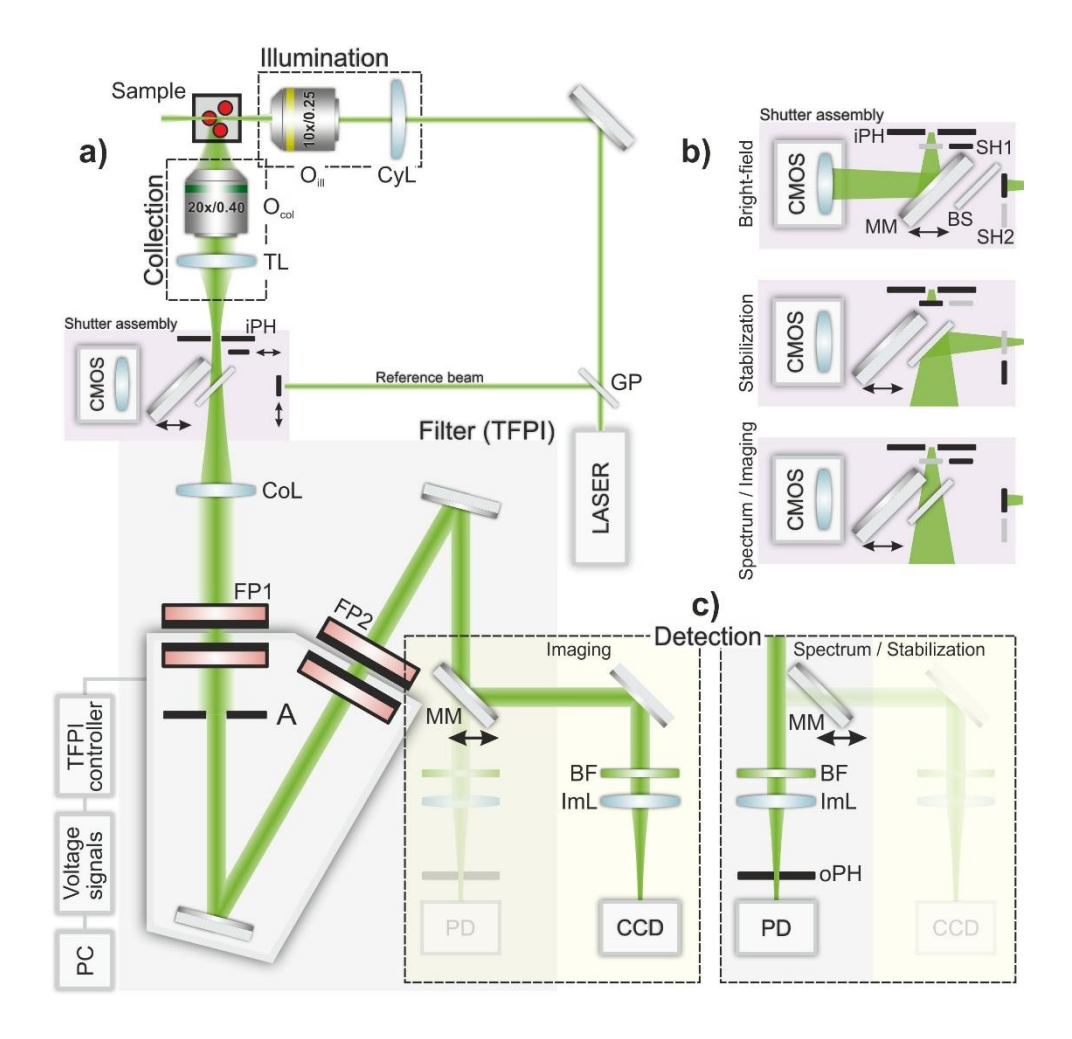


Fig. S2. Optical setup for Full-Field Brillouin Imaging using a Tandem Fabry-Perot **Interferometer** (TFPI). a, The laser beam (Spectra Physics Excelsior, $\lambda = 532 \, \text{nm}$, P = 250 mW, diameter 2 mm) is shaped into a light sheet using a cylindrical lens (CyL, f = 200 mm), which focuses the beam onto the back focal plane of the illumination objective (O_{ill}). Depending on the desired sheet dimensions, either a 50 mm achromatic doublet (Thorlabs AC254-050-A-ML) or a 10× Olympus objective was used. The light sheet illuminates the sample placed near the edge of a 5 × 5 mm rectangular cuvette (Hellma). Light scattered from the illuminated region is collected orthogonally by a detection objective (Ocol, either a 50 mm achromatic doublet, Olympus $20 \times NA = 0.4$, $10 \times NA = 0.25$, or $5 \times NA = 0.13$), and reimaged onto the TFPI input pinhole (iPH) via a tube lens (TL, f = 150 mm, Thorlabs AC254-150-A-ML). An integrated CMOS camera enables bright-field inspection and focusing. The maximum iPH diameter (1 mm) defines the field of view. The light is collimated by the TFPI internal lens (CoL) and passed through two FP cavities (FP1 and FP2) for multi-pass spectral filtering. Internal apertures (A) restrict angular divergence. After passing FP cavities, filtered light reaches the detection module. A small portion of the laser is also redirected as a reference beam for stabilization purposes using a glass plate (GP). b, Operation of the shutter assembly in different modes. Two mechanical shutters (SH1, SH2) control either the measurement beam (via iPH) or the reference beam. **Top**: With SH1 open, the image at iPH is directed to the CMOS camera via a manually movable mirror for bright-field visualization. Middle: In stabilization mode, SH1 is closed and SH2 is opened, sending the reference beam through the TFPI. **Bottom**: In spectral and imaging modes, SH1 is opened, allowing measurement light to pass through the interferometer. c, Two detection modes. Left: In imaging mode, motorized movable mirror MM is inserted into the beam path, and filtered light passes through a band-pass filter (BF) and is

focused onto a CCD camera (FLIR Grasshopper3 GS3-U3-15S5M-C) using an imaging lens (f = 250 mm, Thorlabs AC254-250-A-ML). **Right**: In spectral or stabilization mode, MM is retracted. Light passes through the BF and is focused onto an output pinhole (oPH) by an imaging lens (ImL), then detected by a photodiode (PD).

In FFBI, the entire area of interest must be illuminated simultaneously to avoid spatial scanning. To achieve this, we employed a light-sheet illumination scheme. This configuration is analogous to line-scanning approaches, but extended in the second spatial dimension. A cylindrical lens (f = 200 mm) focuses the laser beam ($\lambda = 532$ nm, P = 250 mW, 2 mm diameter ($1/e^2$)) onto the back focal plane of the illumination objective (O_{iil}), forming a static light sheet. The lens used was either a 50 mm achromatic doublet (Thorlabs AC254-050-A-ML) or a $10\times O$ lympus objective, depending on the required field of view (**Fig. S2a**). When 5mm lens was used the light-sheet has a theoretical width of $500\mu m$, length (Rayleigh range) of $810\mu m$ and thickness (beam waist) of $16\mu m$. The resulting power density (laser power per illuminated volume) was $\sim 0.04\mu W/\mu m^3$. For 10x objective lens the light-sheet dimensions were: width $180\mu m$, length $105\mu m$, thickness (beam waist) of $6\mu m$. The resulting power density was $\sim 2.3\mu W/\mu m^3$.

Scattered light is collected at 90° to the illumination axis, forming an orthogonal-plane geometry. The collection optics include either a 50 mm achromatic doublet (Thorlabs AC254-050-A-ML) or standard microscope objectives: Olympus $5 \times$ (NA = 0.13), $10 \times$ (NA = 0.25), or $20 \times$ (NA = 0.4). The choice of objective determines the spatial resolution and field of view but also distribution of accepted scattering angles [5]. Collected light is relayed through a tube lens (f=150 mm, Thorlabs AC254-150-A-ML) to the input pinhole (iPH) of the TFPI shutter assembly. The sample image is formed at the iPH plane and can be viewed on an integrated CMOS camera for bright-field observation and focus adjustment (**Fig. S2a, S2b top**). The field of view is limited by the circular iPH diameter, which was set to a maximum of 1 mm in our configuration.

The spectral imaging system is built around a TFPI-2 interferometer operating in a six-pass, double-cavity configuration. Light entering the interferometer is collimated and directed through two matched FP cavities (FP1 and FP2). After filtering, the light exits and is routed to one of two detection subsystems via a motorized mirror (MM; Thorlabs MFF101/M) (Fig. S1c). All light passes through a narrow band-pass filter (BF) before detection. In spectral or stabilization mode, light is focused through an output pinhole (oPH; diameter 1.3mm) onto a photodiode. In imaging mode, the beam is focused onto a CCD camera (FLIR Grasshopper3 GS3-U3-15S5M-C) using a 250 mm achromatic doublet (Thorlabs AC254-250-A-ML). To enable imaging, we developed a custom control system allowing external voltage control over all six interferometer axes, shutters (SH1 and SH2) and movable mirror (MM). This system is built using National Instruments DAQ cards and custom LabVIEW code. The mirror spacing was set to 3 mm, yielding a Free Spectral Range (FSR) of 50 GHz, which was found optimal for balancing spectral resolution without lengthening too much optical path.

Modes of Operation

The FSBI system operates in three distinct modes: **stabilization**, **spectral**, and **imaging**. Each mode serves a specific function, and the system is capable of dynamically switching between them during a typical imaging session.

Stabilization Mode

Proper TFPI operation requires optimal alignment of its six degrees of freedom: four mirror tilts (X_1 , Y_1 for the first cavity; X_2 , Y_2 for the second), differential spacing (ΔZ), and the common separation (Z), the latter determines the transmitted frequency. Stabilization mode uses a reference beam, derived by diverting a portion of the laser via a glass plate (GP), which enters the interferometer through a dedicated shutter path (SH2). During this mode, the measurement path (SH1) is closed, and the flip mirror (MM) is retracted, allowing the reference beam to propagate through the interferometer and onto the photodiode via the output pinhole oPH (**Fig. S2b middle**, **S2c right**). A custom-built control system (National Instruments DAQ, LabVIEW interface) adjusts each of the six alignment axes through finesse optimization and drift stabilization routines using well established procedure [6]. The former performs the mirror alignment to ensure maximum transmission through TFPI, while the latter takes care of thermal drifts maintaining transmission frequency of the elastic line (Rayleigh line) at 0 GHz. The full stabilization cycle, including both finesse optimization and drift correction, lasts approximately 1.5 seconds. Under thermally stable conditions, it is sufficient to perform stabilization once every 15 seconds, enabling efficient imaging without frequent interruption.

Spectral Mode

This mode is used to record the integrated Brillouin spectrum from the entire field of view and to define the spectral range to be imaged. The sample is illuminated with the light sheet as usual, and scattered light is collected through the main input (iPH) with SH1 open and the flip mirror retracted. The output pinhole (oPH) is set to maximum 1.3mm to collect light from entire field of view. The system now behaves like a classical scanning spectrometer (Fig. S2b bottom, S2c right). The mirror separation (Z-axis) is scanned over a full Free Spectral Range (FSR), and the transmitted intensity is recorded on the photodiode. The resulting spatially integrated spectrum reveals the position of Brillouin shift for studied material or the number of distinct mechanical features (e.g., multiple peaks). This information is used to define a range of frequencies for the subsequent imaging step. The spectral mode is generally run once for each new sample.

Imaging Mode

In imaging mode, the system switches to CCD detection by inserting the motorized mirror (MM) into the beam path, directing light to the camera (**Fig. S2c, left**). Shutter SH1 is opened to allow measurement light to pass through the TFPI, while SH2 remains closed. Based on the spectral mode results and the known Volt-to-GHz conversion factor, a set of voltage values corresponding to the desired frequency points is generated. Each voltage is applied and held constant during the acquisition of a full-field spectral image. Typical experiments involved collecting 40 images, covering both Stokes and anti-Stokes sides. Depending on the camera pixel binning (2× or 1×), the integration time per spectral image ranged from 0.5 to 2 seconds, with the fixed field of view sampled by either ~100 or ~200 pixel radius, respectively. The total acquisition time for a full stack of spectral images was 30–80 seconds. Faster acquisition could be achieved by reducing the number of spectral points or limiting imaging to one side of the Brillouin spectrum. Thermal and mechanical stability were sufficient to complete multi-image acquisitions with only occasional re-stabilization.

3. Data Processing

To extract spatially resolved mechanical properties from full-field Brillouin imaging, we implemented a two-step data analysis procedure. The first approach uses classical fitting of Brillouin spectra with a damped harmonic oscillator (DHO) model. The second, more advanced method corrects for optical distortions allowing recovery of absolute mechanical properties.

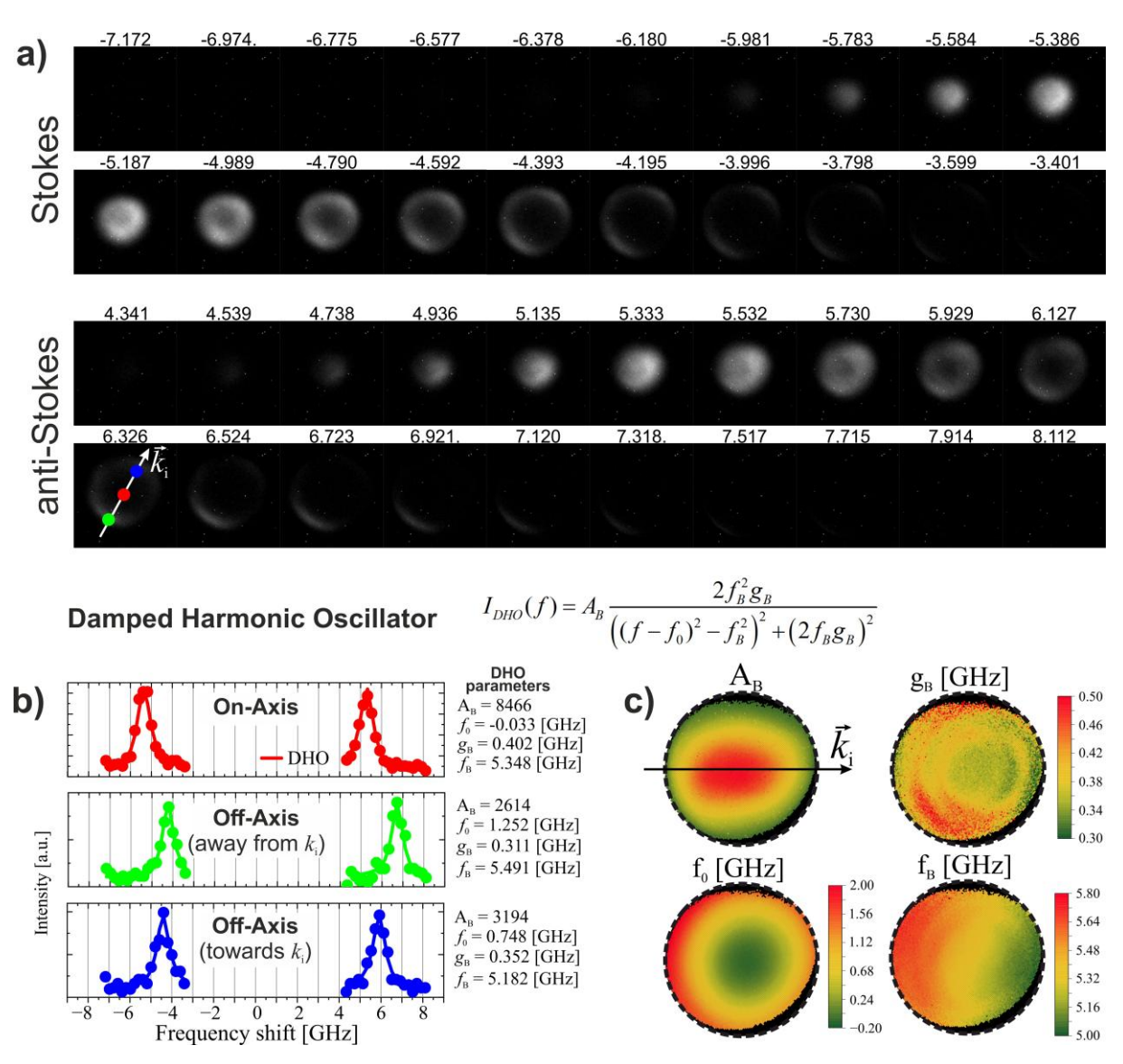


Fig. S3. Brillouin spectra from spectral image stacks. **a**, Raw spectral images of water for both Stokes and anti-Stokes regions, with frequency shift (GHz) indicated above each frame. White arrow shows the incident beam direction k_i . Colored markers identify pixels analyzed in panels b and c. **b**, Brillouin spectra from the red, blue, and green pixels in (a), with DHO fits (Eq. S9). Corresponding fit parameters are listed. **c**, Maps of DHO fit parameters (A_B , f_B , g_B , f_0) across the field of view.

Classical DHO-Based Spectral Fitting

In the standard approach, the Brillouin spectrum for each pixel is reconstructed by collecting intensity values from the stack of spectral images recorded at discrete frequencies near the Brillouin shift. This results in a one-dimensional spectrum for each spatial location (pixel), which is then fit using the DHO model:

$$I_{DHO}(f) = A_B \frac{2f_B^2 g_B}{\left((f - f_0)^2 - f_B^2 \right)^2 + \left(2f_B g_B \right)^2}$$
 (S9)

Here, A_B is the integrated amplitude of the Brillouin line, f_B is the Brillouin frequency shift, g_B is the Brillouin line width (half-width at half-maximum, HWHM), and f_0 is the frequency offset. Example results from a homogeneous water sample are shown in **Fig. S3**. Panel **S3a** displays raw spectral images from both Stokes and anti-Stokes regions. Each image corresponds to a specific frequency, with shifts indicated above. Three selected pixels are marked—red (on optical axis), blue (along illumination direction), and green (opposite to illumination)—to demonstrate spatial dependence of the signal. Corresponding Brillouin spectra for these positions and their DHO fits are shown in **S3b**, illustrating spectral variation. The fitted DHO parameters across the field of view are mapped in **S3c**. Notably, even in a homogeneous sample like water, spatial variations are observed—indicating artifacts related to spatial distribution of the FPI cavity errors and potential interferometer misalignment [7].

Precision in Brillouin shift and line-width

The spectral precision of the instrument was evaluated by analyzing repeated measurements of a static, homogeneous sample (pure water) [8]. Following the procedure described in the previous section—pixel-wise fitting of the damped harmonic oscillator (DHO) model spatial maps of the Brillouin shift f_B and the Brillouin line width g_B were generated for 7 independent measurements. Representative maps for single measurement are shown in **Fig.S4a** and **Fig.S4d** respectively. Both parameters exhibit spatial inhomogeneities: f_B displays a characteristic directional tilt, while the g_B map shows more complex structure.

Spectral precision was assessed using two approaches: per-pixel precision and field-of-view (FOV)—averaged precision. For per-pixel precision, the standard deviation (σ) across the seven measurements was calculated at each pixel, resulting in spatial maps of σ_{fB} and σ_{gB} shown in **Fig.S4b** and **Fig.S4e**. Precision varies across the FOV, with central pixels showing deviations of ~15 MHz for both f_B and g_B , and increasing toward the edges, reaching ~50 MHz. Relative to mean values of f_B ~5.3 GHz and g_B ~0.4 GHz, these correspond to relative errors of ~0.4% and ~5%, respectively. The spatial variation in precision closely follows the signal-to-noise ratio (SNR) distribution, shown in **Fig.S4g**. SNR was calculated as the ratio of the RMS amplitude of the Brillouin peak to the RMS noise floor, following the procedure described in [9]. The SNR ranges from >30 dB at the FOV center to ~15 dB at the edges. The observed relationship between precision and SNR follows the well-established behavior known for Brillouin light scattering (BLS) systems [9]. For the FOV-averaged precision, histograms of f_B and g_B values from each measured map were constructed and are shown in **Fig.S4c** and **Fig.S4f**, respectively. The g_B histogram was well-fitted with a Gaussian profile, yielding a standard

deviation of ~50 MHz, which corresponds to a relative FOV error of ~13%. A similar analysis was not performed for f_B due to the directional tilt across the FOV, which results in a quasi-uniform distribution. However, as the f_B values are less affected by the spatial artifacts observed in the g_B maps, we expect that its FOV-averaged precision is comparable to the per-pixel estimate.

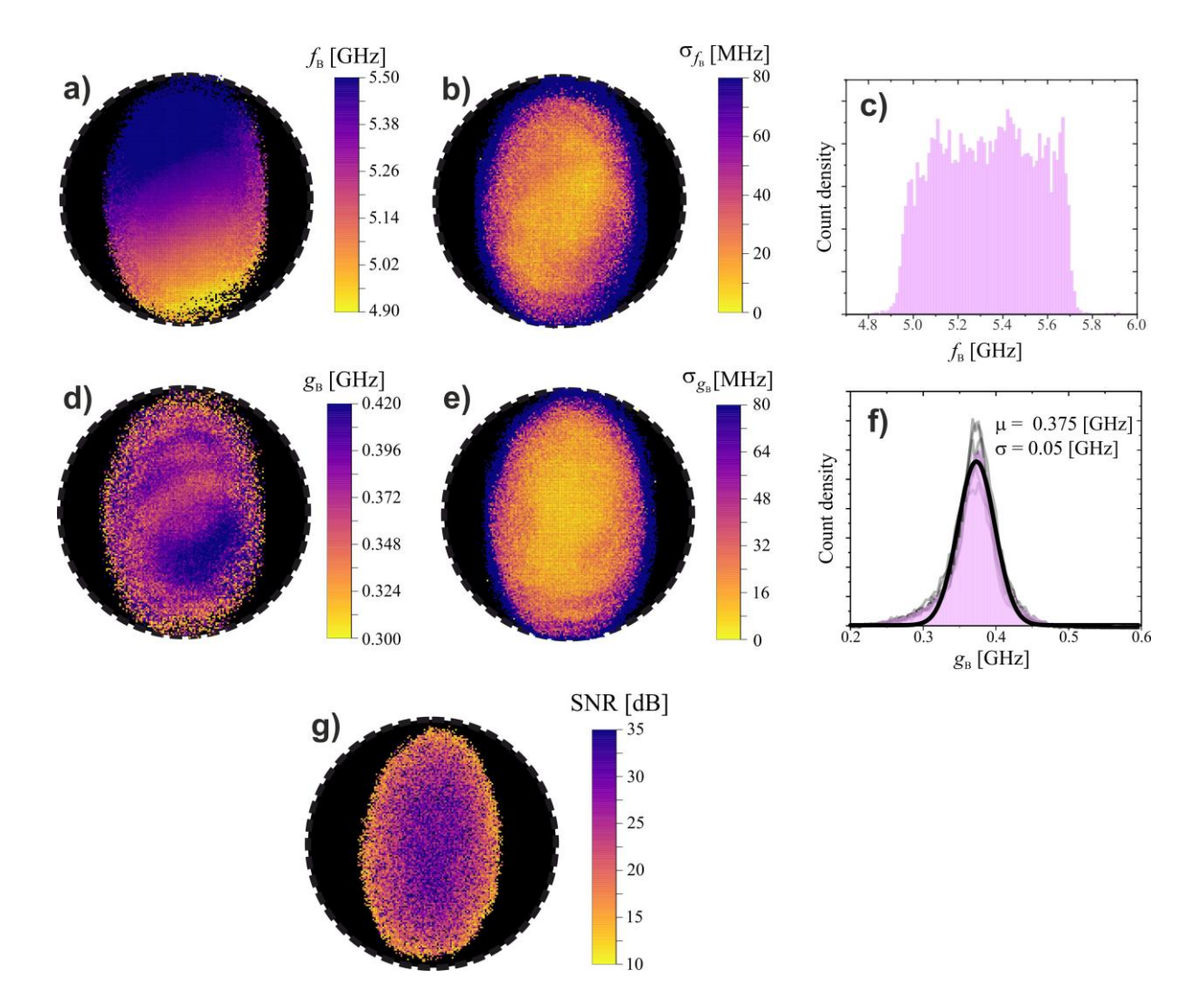


Fig. S4. Spectral precision of Brillouin shift and linewidth measurements. a, Spatial map of Brillouin shift (f_B) extracted from a single measurement of pure water, showing characteristic directional tilt due to optical geometry. **b**, Per-pixel standard deviation of f_B across seven independent measurements, representing local measurement precision. **c**, Histogram of f_B values aggregated over the field of view from all measurements, showing quasi-uniform distribution resulting from spatial spread of shift values. **d**, Spatial map of Brillouin linewidth (g_B) from a single measurement, showing spatial non-uniformities. **e**, Per-pixel standard deviation of g_B across repeated measurements, indicating linewidth precision. **f**, Histogram of g_B values fitted with a Gaussian distribution, used to estimate field-averaged precision. Histograms from each individual measurement is presented as gray lines. The average distribution from all measurements is presented as shaded area. Black line is a Gaussian fit. **g**, Signal-to-noise ratio (SNR) map for the same dataset, showing correspondence between SNR and local spectral precision.

Scattering Angle-Corrected Analysis for Mechanical Quantification

While the Brillouin shift f_B is often used as a proxy for mechanical properties, the actual quantity of interest is the speed of sound c_B , which is directly related to elastic modulus or compressibility (eq.S1). The Brillouin shift is related to the magnitude of acoustic wave-vector q, which depends on the scattering angle θ (eq.S3). Because light is collected over a range of angles (because of microscope objective finite numerical aperture), the measured Brillouin spectrum I(f) represents a weighted sum of many scattering events (each occurring at certain scattering angle θ):

$$I(f) = \int_{0}^{\pi} I_{DHO}(f,\theta) p(\theta) d\theta$$
 (S10)

The single-angle DHO spectrum $I_{DHO}(f,\theta)$

$$I_{DHO}(f,\theta) = A_B \frac{2f_B^2(\theta)g_B(\theta)}{\left((f - f_0)^2 \pm f_B^2(\theta)\right)^2 + \left(2f_B(\theta)g_B(\theta)\right)^2}$$
(S11)

accounts for how both, Brillouin shift and width, vary with θ :

$$f_B(\theta) = \frac{1}{2\pi} nc_B q_n(\theta)$$
 (S12)

$$g_B(\theta) = \frac{1}{4\pi} n^2 \eta_B q_n^2(\theta) \tag{S13}$$

To facilitate data interpretation without knowing the refractive index n, we are using reduced quantities (S6-S8). The angular distribution $p(\theta)$ is modeled as a Gaussian:

$$p(\theta) = \frac{1}{\sqrt{2\pi\sigma_{\theta}^2}} \exp\left(-\frac{\left(\theta - \theta_m\right)^2}{2\sigma_{\theta}^2}\right)$$
 (S14)

We assume that in the relevant frequency range no structural relaxation occurs, so both c_B and η_B are independent of q. Spectral broadening caused by both angular averaging and interferometer limited resolution is combined into the $p(\theta)$ term.

Two-Step Inversion Strategy

The full inversion consists of:

- 1. **Calibration**: A reference sample (e.g., pure water) with known nc_B and $n^2\eta_B$ is used to determine scattering angle distribution maps $\theta_m(x,y)$ and $\sigma_\theta(x,y)$ by fitting Eq. S10 to experimental spectra. Only A_B , f_0 , θ_m , σ_θ are free parameters.
- 2. **Material Property Extraction**: With angular maps fixed, Brillouin spectra from an unknown sample are fitted using the same model (Eq.S10), but with A_B , f_0 , nc_B , $n^2\eta_B$ as

free parameters. This yields spatially resolved maps of reduced acoustic and viscoelastic properties.

To assess precision, pure water was used both for calibration and property extraction in two separate measurements. Results are shown in **Fig. S5**. In **Fig.S5a**, model fits to representative Brillouin spectra from three spatial points (the same as on **Fig.S3a,b**) are shown alongside their corresponding scattering angle distributions in **Fig.S5b**. **Fig.S5c** presents spatial maps of θ_m and σ_θ across the field of view. Using these calibrations, we extracted nc_B and $n^2\eta_B$ from a second dataset of water, shown in **Fig.S5d–e**. Histograms from ten independent measurements are included to demonstrate reproducibility.

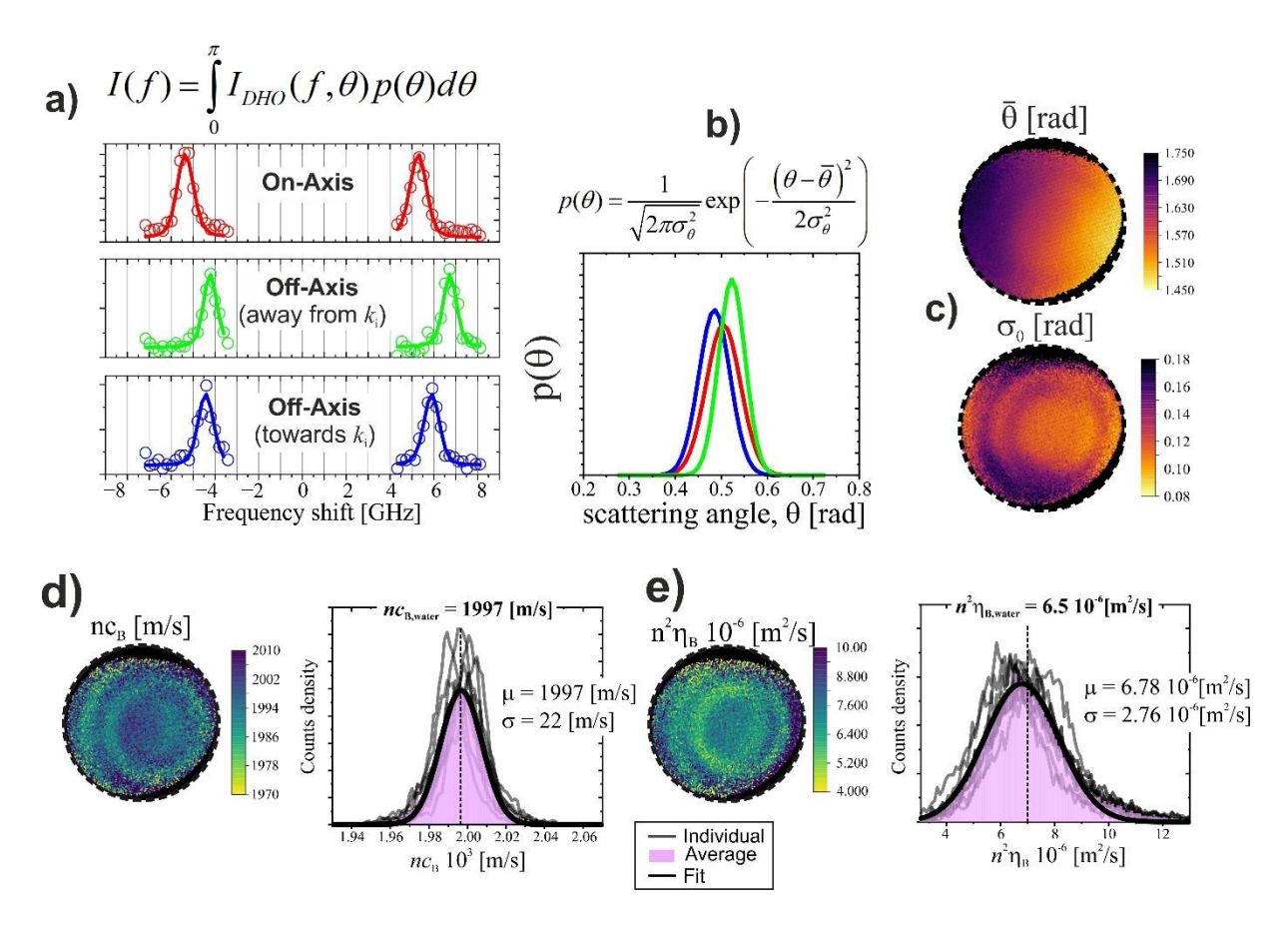


Fig. S5. Angular deconvolution for quantitative mechanical mapping. a, Example Brillouin spectra from three pixels (marked in Fig. S3a), fitted using Eq. S10 with a Gaussian scattering angle distribution. b, Scattering angle distributions $p(\theta)$ corresponding to spectra in (a). c, Calibration maps of scattering angle distributions parameters—mean scattering angle θ_m (top) and standard deviation σ_θ (bottom)—obtained from fitting Eq. S10 to water spectra with fixed mechanical properties. d,e, Retrieved spatial maps and histograms of reduced speed of sound nc_B (d) and reduced longitudinal viscosity $n^2\eta_B$ (e) from independent test data using the calibration from (c). Gray lines show results from ten separate datasets; the mean histogram (shaded area) is fitted with a Gaussian (black curve).

Using mean and standard deviation values from histograms of acoustic parameters (**Fig.S5d** and e), the estimated relative FOV errors in estimation of acoustic parameters are ~1% and ~40% for ncB and $n_2\eta B$, respectively.

Comparing these values with earlier presented spectral precision (\sim 0.4% for f_B and \sim 13% for g_B), it is clear that numerical manipulation is responsible for almost 3x reduction is acoustic precision as compared to spectral precision.

4. Consequences of Suboptimal FPI Design and Rationalization of Spectral Measurement Outcomes

The Tandem Fabry–Perot Interferometer (TFPI) employed in our setup was not originally intended for imaging. Its design prioritizes transmission of collimated, on-axis beams for single-point Brillouin spectroscopy, with long internal optical paths and angularly restrictive apertures deliberately introduced to maximize contrast and resolution. The adaptation of this architecture for full-field imaging comes with a series of predictable but manageable artifacts.

Figure S6 provides a graphical breakdown of the origin and nature of these effects. Panel **a** shows the two major functional blocks of the system: the microscope unit, which produces a magnified image of the illuminated sample plane; and the filter unit, which performs spectral selection and forms the final image on the CCD camera.

Panel **b** details light propagation from a single point in the sample through the microscope unit. Due to the finite numerical aperture (NA) of the collection objective, light scattered at a range of angles is collected. These correspond to different magnitudes of wave-vectors q, each encoding a different Brillouin shift. The critical point is that these angular components are spatially separated within the collimated region of the optical path. The light scattered at perfect 90° propagates along the optical axis, while lower- and higher-angle rays are displaced in opposite directions—shifted toward or away from the incident beam vector \mathbf{k}_i , respectively.

Panel **c** explains the consequences of this angular spread when light enters the filter unit. Internal apertures within the TFPI restrict beam divergence, thereby acting as spatial filters. Rays from different image positions (e.g., "+1" or "-1") experience selective attenuation of part of their angular distribution—cutting off high- or low-q components, respectively. At the same time, the Fabry–Perot interferometer performs narrow-band spectral filtering. The effective optical path length increases for beams entering the cavity at an angle, shifting the resonance frequency. This leads to the observed parabolic offset in spectral maps of f_0 , where the center frequency of the Brillouin line varies symmetrically with field position (**Fig.S3c** and profile in **Fig.1b**). These combined effects also cause the formation of ring-like structures in single-frequency images (**Fig.S3a**), as only a circular subset of rays meets the transmission condition at any given mirror separation.

Panel **d** illustrates how these effects translate to spatial artifacts in the Brillouin spectral maps. Because each pixel receives light corresponding to a distribution of scattering vectors δq , the recorded Brillouin spectrum is an average over this distribution. The shift f_B recorded at the image center reflects the full angular spread and is closest to the actual value. Moving along the illumination axis, filtering skews the q-distribution: low-q values are lost in one direction, high-q in the other. This results in a tilted plane across the field of view in the spatial map of f_B , even for homogeneous samples (**Fig.S3c** and profile in **Fig.1b**). Meanwhile, the linewidth g_B is expected to narrow at off-axis positions due to angular filtering—but this is often obscured by a concurrent loss of finesse in the interferometer, especially for oblique rays, which degrades spectral resolution and can artificially broaden the peaks. This rationalize substantial uncertainty in linewidth-derived metrics (**Fig.S5e**).

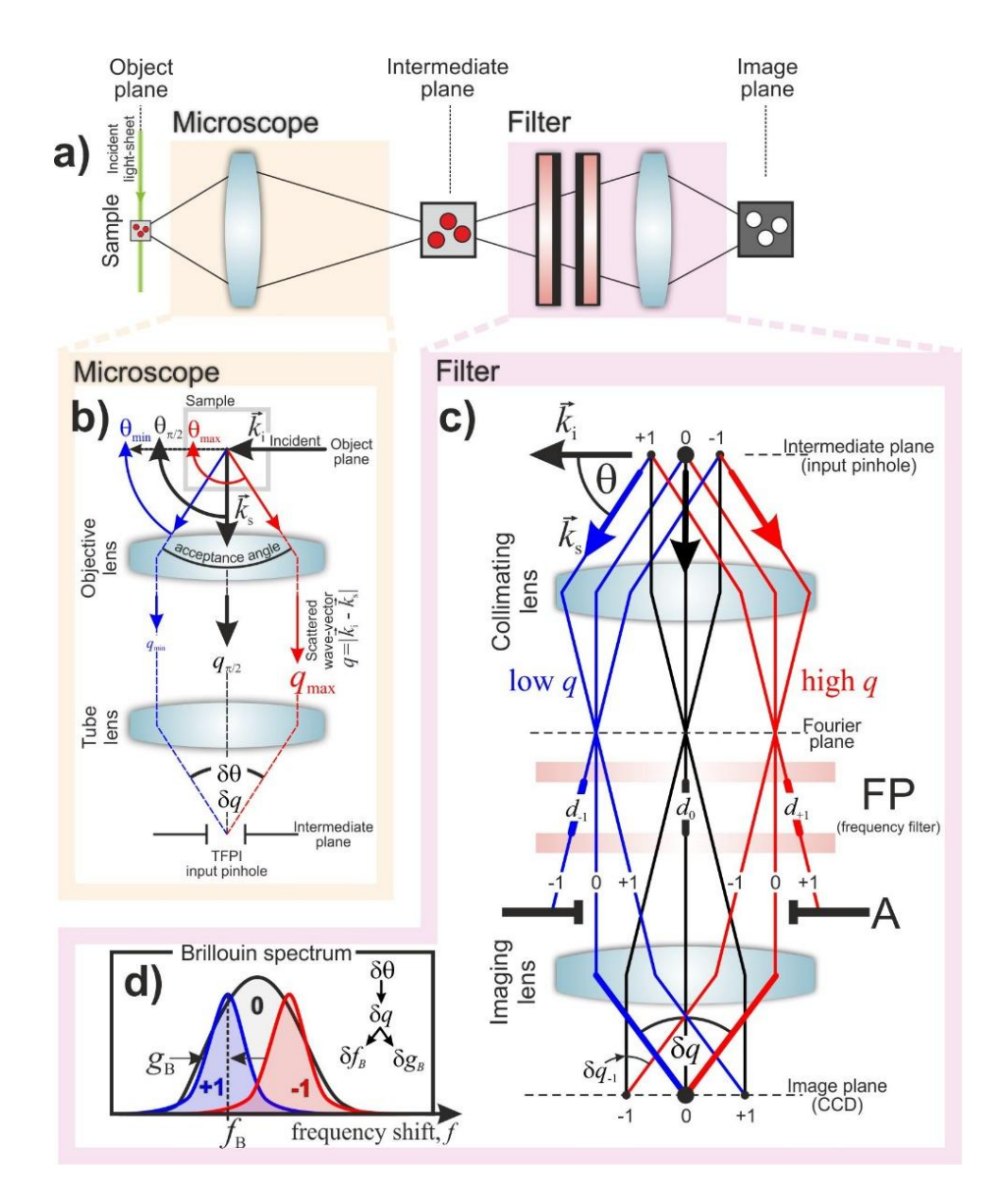


Fig. S6. Light propagation and artifacts in Full-Field Brillouin Imaging with a Fabry-Perot interferometer. a, Schematic overview of the optical system, divided into two main modules: the microscope unit and the Fabry-Perot (FP) filter unit. The microscope's role is to form a magnified image of the sample plane (illuminated by a light sheet) at the input pinhole of the interferometer. The filter unit spectrally selects the transmitted frequency components and projects a filtered image onto the CCD camera. b, Light propagation through the microscope unit from a single point in the field of view. Scattered radiation collected by the microscope objective contains a distribution of scattering angles (or wave-vectors q) due to the finite numerical aperture (NA). Light scattered at perfect 90° ($\theta = \pi/2$) travels along the optical axis. Rays scattered at lower angles (smaller q, denoted q_{\min}) propagate shifted in the direction of the incident beam vector k_i ; higher-angle rays (larger q, q_{max}) shift oppositely. This causes spatial separation of angular components in the collimated beam. c, Light propagation through the filter unit. The extended image at the input pinhole forms an off-axis light source. Rays from different positions in the field of view (e.g., center "0", and points "+1" or "-1" along the illumination axis) enter the filter with distinct angular shifts. Internal apertures (A) limit beam divergence and thus introduce spatial filtering, suppressing part of the angular distribution differently across the field. The rays propagate through FP interferometer, which acts as a

tunable narrow-band filter. Due to angled incidence, off-axis rays encounter effectively longer mirror separations (denoted d_{+1} , d_{-1}) compared to the on-axis beam d_0 , shifting the frequency of maximum transmission (cosine dependence). **d**, Conceptual explanation of how the spatial filtering of angular components modifies the recorded Brillouin spectrum. The objective collects a distribution δq of scattering vectors, translating to a distribution of Brillouin shifts δf_B and linewidths δg_B . These are averaged in the detected signal. For the central point "0", the full angular distribution is preserved. For point "+1", high-q components are blocked, leading to lower average f_B . For point "-1", low-q components are blocked, resulting in higher f_B . This angularly dependent filtering leads to the observed plane-shaped variation in f_B maps (**Fig.S3c**). Expected narrowing of the linewidths g_B at off-axis positions is often obscured by degradation of finesse and signal loss in the FP, which may counteract any narrowing due to angular restriction.

5. Estimating Spatial Resolution

To evaluate the spatial resolution of the Full-Field Brillouin Imaging system, we performed experiments on a heterogeneous sample composed of two mechanically distinct materials—PMMA and water—positioned adjacent to each other. Brillouin imaging of this sharp interface allows the resolution to be quantified by analyzing the steepness of the transition between materials.

Two independent methods were used to estimate the resolution, each based on a different processing approach.

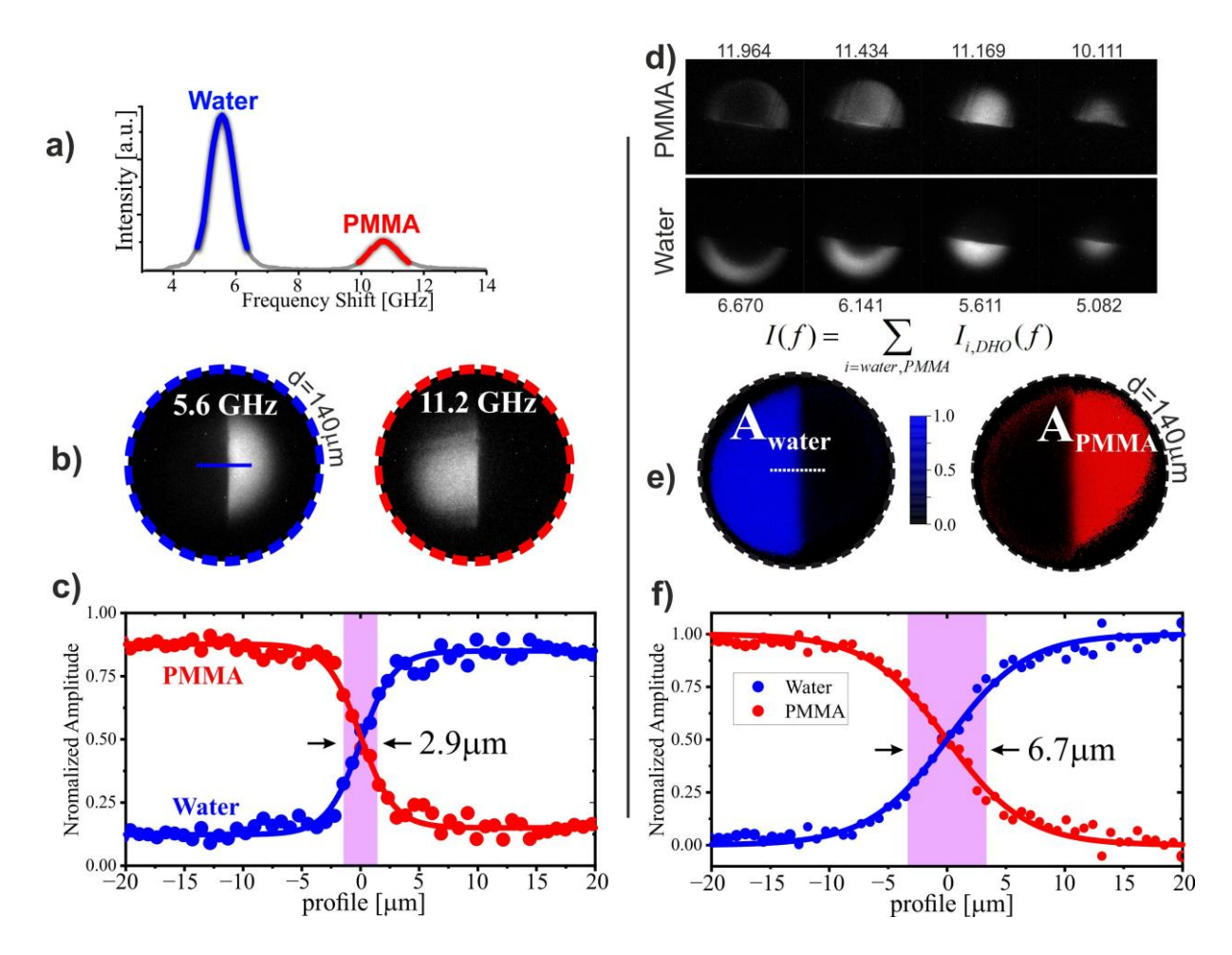


Fig. S7. Two approaches to estimating spatial resolution in full-field Brillouin imaging. a, Integrated anti-Stokes Brillouin spectrum acquired from a sample composed of two materials with distinct mechanical properties: PMMA and water. The spectrum shows two well-separated Brillouin peaks—at lower frequency for water (blue) and at higher frequency for PMMA (red). b, Spectral images recorded at frequencies corresponding approximately to the maxima of each Brillouin peak. Each image displays a clear spatial separation between the two materials. The circular field of view is 140 µm in diameter. c, Intensity profiles along the boundary between the two regions (extracted along the blue line in panel b) show a sharp transition. Profiles were fit with a Boltzmann sigmoid function to estimate the full width at half maximum (FWHM) of the transition zone. d, Series of spectral images on the anti-Stokes side of the Brillouin spectrum at selected frequencies (indicated above each image). These were used to reconstruct the full Brillouin spectrum at each pixel. e, Spatial maps of the normalized Brillouin amplitude for water and PMMA components, obtained by fitting the pixel-wise spectra with a sum of two damped harmonic oscillator (DHO) functions. A distinct mechanical boundary is observed, similar to panel b. f, Normalized amplitude profiles extracted across the boundary in panel e (along the dashed line) and fitted with Boltzmann sigmoid functions. The resulting FWHM values are larger than those estimated by the first method (panels a-c), highlighting methoddependent differences in spatial resolution.

In the first method, resolution was assessed directly from individual spectral images. As shown in **Fig. S7a**, the integrated Brillouin spectrum of the entire field of view reveals two distinct peaks corresponding to water (lower frequency, blue) and PMMA (higher frequency, red).

Spectral images were recorded with the interferometer tuned to each peak (**Fig. S7b**). These images exhibit a clear boundary between the two materials. A horizontal line profile taken across the interface (blue line in panel b) is plotted in **Fig. S7c**. Fitting this profile with a Boltzmann sigmoid function yields the full width at half maximum (FWHM), which serves as a measure of spatial resolution. The result from this method indicates a resolution of approximately 3 μ m.

The second method derives spatial resolution from full spectral reconstruction and analysis of Brillouin amplitudes. A sequence of spectral images spanning both the Stokes and anti-Stokes sides of the Brillouin spectrum was acquired (only the anti-Stokes images are shown in Fig. S6d for clarity). Using the approach described in the Data Processing section (and **Fig. S3**), Brillouin spectra were reconstructed at each pixel and fit with a sum of two damped harmonic oscillator (DHO) functions—one for each material. From the resulting fits, spatial maps of Brillouin line amplitudes ($A_{B,water}$ and $A_{B,PMMA}$) were extracted for both PMMA and water components (**Fig. S7e**). These amplitude (normalized) maps also show a distinct mechanical interface. Profiles taken across the boundary (along the dashed line in panel e) are shown in **Fig. S7f** and similarly fitted with Boltzmann functions to extract the FWHM. This second method yields a broader transition width of approximately 7 μ m.

6. Performance comparison of selected Brillouin imaging systems

Table S1. Comparison of performance metrics for selected Brillouin imaging systems: Full-field approaches with Fabry-Perot interferometer (FPI) and Fourier-transform spectrometer (FT), Line-scanning Brillouin microscopy (LSBM), Confocal Brillouin microscopy (CBM) and Brillouin gain microscopy (BGM).

	Full-field (FPI)	Full-field (FT) ^[1]	LSBM ^[2]	CBM ^[3]	BGM ^[4]
Laser wavelength [nm]	532	780	780	532 / 660	780
Laser power [mW]	250	56	20 / 370	2-61	230
Illuminated volume [μm³]	~450.000 ^[7]	~1.700.000 ^[8]	~300 ^[9] / 2000 ^[10]	~0.1 ^[11]	0.18 ^[11]
Power density ^[5] [mW/μm ³]	~5 10-4	~3 10 ⁻⁵	~10 ⁻¹	20 - 600	~1300
Spectrum integration time [ms]	30.000 - 80.000	15.000	100 - 200	20-250	0.1
Number of multiplexed spectra	30.000	450.000	100 - 200	1	1
Effective pixel dwell time [ms]	1-2	0.03	1	20-250	0.1
Effective energy density ^[6] [μJ/μm ³]	~10 ⁻³	~10 ⁻⁶	~10 ⁻¹	~104	~10 ²
SNR [dB]	~15 ->30	~24 ^[12]	~24-29	~24-29	~30
Precision in Brillouin shift [MHz]	~15-50	~70	~10-20	~10	6

^[1] Data taken from reference [10]

^[2] Data taken from reference [11,12]

^[3] Data taken from reference [13–15]

^[4] Data taken from reference [16].

^[5] Defined as power delivered to illuminated volume

^[6] Defined as power delivered to illuminated volume during effective pixel dwell time

^[7] Estimated from light-sheet dimensions: 180µm x 210µm x 12µm

^[8] Estimated from light-sheet dimensions: 598µm x 287µm x 10µm

^[9] Estimated from line dimensions: line diameter=1.5µm, line length=170µm [12])

- [10] Estimated from line dimensions: line diameter 4µm, line length =150µm [11])
- [11] Estimated from optical resolution (Supplementary Table 2. in reference [16]
- [12] Estimated from reconstructed spectrum shown in Extended Data Fig. 3a [10]

References:

- 1. F. Palombo and D. Fioretto, "Brillouin Light Scattering: Applications in Biomedical Sciences," Chem. Rev. **119**, 7833–7847 (2019).
- 2. B. J. Berne and R. Pecora, *Dynamic Light Scattering*. (Wiley, 1976).
- 3. M. Merklein, I. V. Kabakova, A. Zarifi, and B. J. Eggleton, "100 years of Brillouin scattering: Historical and future perspectives," Appl. Phys. Rev. 9, 041306 (2022).
- 4. J. R. Sandercock, "Simple stabilization scheme for maintenance of mirror alignment in a scanning February-Perot interferometer," J. Phys. [E] **9**, 566–569 (1976).
- 5. G. Antonacci, M. R. Foreman, C. Paterson, and P. Török, "Spectral broadening in Brillouin imaging," Appl. Phys. Lett. **103**, 221105 (2013).
- 6. B. Hillebrands, "Progress in multipass tandem Fabry–Perot interferometry: I. A fully automated, easy to use, self-aligning spectrometer with increased stability and flexibility," Rev. Sci. Instrum. **70**, 1589–1598 (1999).
- 7. K. P. Reardon and F. Cavallini, "Characterization of Fabry-Perot interferometers and multi-etalon transmission profiles: The IBIS instrumental profile," Astron. Astrophys. **481**, 897–912 (2008).
- 8. P. Bouvet, C. Bevilacqua, Y. Ambekar, G. Antonacci, J. Au, S. Caponi, S. Chagnon-Lessard, J. Czarske, T. Dehoux, D. Fioretto, Y. Fu, J. Guck, T. Hamann, D. Heinemann, T. Jähnke, H. Jean-Ruel, I. Kabakova, K. Koski, N. Koukourakis, D. Krause, S. La Cavera, T. Landes, J. Li, H. Mahmodi, J. Margueritat, M. Mattarelli, M. Monaghan, D. R. Overby, F. Perez-Cota, E. Pontecorvo, R. Prevedel, G. Ruocco, J. Sandercock, G. Scarcelli, F. Scarponi, C. Testi, P. Török, L. Vovard, W. J. Weninger, V. Yakovlev, S.-H. Yun, J. Zhang, F. Palombo, A. Bilenca, and K. Elsayad, "Consensus statement on Brillouin light scattering microscopy of biological materials," Nat. Photonics 19, 681–691 (2025).
- 9. G. Yan, A. Bazir, J. Margueritat, and T. Dehoux, "Evaluation of commercial virtually imaged phase array and Fabry-Pérot based Brillouin spectrometers for applications to biology," Biomed. Opt. Express 11, 6933 (2020).
- 10. C. Bevilacqua and R. Prevedel, "Full-field Brillouin microscopy based on an imaging Fourier-transform spectrometer," Nat. Photonics **19**, 494–501 (2025).
- 11. J. Zhang, M. Nikolic, K. Tanner, and G. Scarcelli, "Rapid biomechanical imaging at low irradiation level via dual line-scanning Brillouin microscopy," Nat. Methods **20**, 677–681 (2023).
- 12. C. Bevilacqua, J. M. Gomez, U.-M. Fiuza, C. J. Chan, L. Wang, S. Hambura, M. Eguren, J. Ellenberg, A. Diz-Muñoz, M. Leptin, and R. Prevedel, "High-resolution linescan Brillouin microscopy for live imaging of mechanical properties during embryo development," Nat. Methods **20**, 755–760 (2023).
- 13. G. Scarcelli, W. J. Polacheck, H. T. Nia, K. Patel, A. J. Grodzinsky, R. D. Kamm, and S. H. Yun, "Noncontact three-dimensional mapping of intracellular hydromechanical properties by Brillouin microscopy," Nat. Methods **12**, 1132–1134 (2015).

- 14. C. Bevilacqua, H. Sánchez-Iranzo, D. Richter, A. Diz-Muñoz, and R. Prevedel, "Imaging mechanical properties of sub-micron ECM in live zebrafish using Brillouin microscopy," Biomed. Opt. Express **10**, 1420–1431 (2019).
- 15. M. Nikolić and G. Scarcelli, "Long-term Brillouin imaging of live cells with reduced absorption-mediated damage at 660nm wavelength," Biomed. Opt. Express **10**, 1567–1580 (2019).
- 16. R. Shaashoua, L. Kasuker, M. Kishner, T. Levy, B. Rotblat, A. Ben-Zvi, and A. Bilenca, "Brillouin gain microscopy," Nat. Photonics **18**, 836–841 (2024).